Journal of Industrial and Engineering Chemistry 109 (2022) 125–136

Contents lists available at ScienceDirect

Journal of Industrial and Engineering Chemistry

journal homepage: www.elsevier.com/locate/jiec

Effects of hydrothermal parameters on the physicochemical property and photocatalytic degradation of bisphenol A of Ti-based TiO_2 nanomaterials

Dong Li [a], Yunzhou Chen [a], Jialin Jia [b,*], Haiyang He [b], Wei Shi [b,c], Jianghua Yu [a], Jun Ma [b]

[a] Collaborative Innovation Center of Atmospheric Environment and Equipment Technology, Jiangsu Key Laboratory of Atmospheric Environment Monitoring and Pollution Control, School of Environmental Science and Engineering, Nanjing University of Information Science & Technology, Nanjing 210044, China
[b] State Key Laboratory of Urban Water Resource and Environment, School of Environment, Harbin Institute of Technology, Harbin 150090, China
[c] China Everbright Water Limited, China

ARTICLE INFO

Article history:
Received 12 August 2021
Revised 6 January 2022
Accepted 28 January 2022
Available online 4 February 2022

Keywords:
Ti-based TiO_2 nanomaterials
Hydrothermal parameters
Ostwald ripening
Physicochemical property
Photocatalytic activity

ABSTRACT

Effects of hydrothermal parameters on morphology, crystal structure, light absorption, separation efficiency of photo-generated charge carriers, and photocatalytic removal of Bisphenol A (BPA) of Ti-based TiO_2 nanomaterials were systematically investigated. Through changing hydrothermal parameters, TiO_2 nanobelts, TiO_2 nanosheets and TiO_2 nanowires were prepared. With increasing NaOH concentration, hydrothermal temperature, and hydrothermal time, more TiO_2 with (101) crystal plane grew on Ti substrate, resulting in higher crystallinity. The UV-light absorption enhanced with increasing NaOH concentration, but decreased with improving hydrothermal temperature, hydrothermal time, and HCl concentration. Variation of UV-light absorption was mainly affected by morphology, and UV-light absorption of TiO_2 nanomaterials with different morphologies was arranged in order of nanobelts > nanosheets > nanowires. The hydrothermal growth of TiO_2 nanomaterials on Ti plate conformed to Ostwald ripening mechanism. Variation trend of photo-generated current was consistent with that of BPA degradation, they both first increased and then decreased within investigated range. The optimal NaOH concentration, hydrothermal temperature, hydrothermal time, and HCl washing concentration were 1 M, 170℃, 28 h, and 0.1 M, respectively. Under this condition, Ti-based TiO_2 nanosheets exhibited the highest BPA removal efficiency (92.7%), which was due to highly ordered nanosheet structure, good crystallinity, appropriate UV-light absorption and high separation efficiency of electron-hole pairs.

Introduction

Over the past decades, the photocatalytic advanced oxidation technology based on TiO_2 nanomaterials has been extensively developed in the fields of air and water purification [1–6]. However, practical application of TiO_2 nanomaterials for purifying water is greatly limited because of its inherent drawback that the pulverous TiO_2 catalyst is difficult to separate and recycle in the suspended aqueous solution [7]. Therefore, it may cause catalyst loss and secondary pollution of treated water. To conquer this, numerous approaches have been performed to immobilize TiO_2, such as sol–gel spin or brush coating method [8,9], chemical vapor deposition [10], in situ growth on Ti plate by the anodization or hydrothermal treatment [11,12], and so on [13]. Among them, direct growth of TiO_2 on Ti substrate has become one of the most effective ways for preparing TiO_2 catalyst owing to their chemical bonding [11].

Generally, surface micro-morphology of Ti-based TiO_2 nanomaterials significantly affected its separation efficiency of photo-generated charge carriers and photocatalytic activity [14]. There are many Ti-based TiO_2 nanomaterials with various morphologies that had been synthesized and used for water remediation, including nanowires [15,16], nanotubes [17,18], nanobelts [19] and nanorods [20], and nanosheets [21–23]. For instance, vertically orientated TiO_2 nanotubes arrays by anodization of Ti substrate can provide an effective nano-architecture for charge transfer and improvement of photocatalytic efficiency [17,18]. Wang et al. [22] prepared Ti-based TiO_2 nanosheets film by an alkaline hydrothermal reaction and concluded that TiO_2 nanosheets pos-

* Corresponding author at: State Key Laboratory of Urban Water Resource and Environment, School of Environment, Harbin Institute of Technology, Harbin 150090, China.
E-mail address: huaiqiu1234@126.com (J. Jia).

https://doi.org/10.1016/j.jiec.2022.01.032
1226-086X/

sess a higher photocatalytic efficiency than that of TiO_2 nanotubes prepared by the anodization. Our previous study [23] reported that Ti-based TiO_2 nanomaterials with various morphologies were prepared at different hydrothermal temperature. It was found that TiO_2 nanosheets exhibited an enhanced separation efficiency of charge carriers compared to TiO_2 nanobelts and TiO_2 nanowires. Therefore, alkaline hydrothermal process has been considered as one of the versatile candidates for preparation of Ti-based TiO_2 nanomaterials due to its controllable morphology and outstanding photocatalytic activity.

For the alkaline hydrothermal method, $Na_2Ti_3O_7$ is first generated and then the Na^+ ions are exchanged with H^+, followed by heat treatment to produce TiO_2 nanomaterials [21,23]. In addition to Ti substrate (foil and plate), TiO_2/P25 (Degussa) or other precursors (titanium isopropoxide, tetrabutyl titanate, $TiCl_4$, etc) have been widely used to prepare powder TiO_2 nanomaterials via alkaline hydrothermal process [24]. The morphology and properties of TiO_2 nanomaterials are affected greatly by the hydrothermal parameters, including temperature, NaOH concentration, time and acid washing. In general, increase in hydrothermal temperature will provide a strong driving force for hydrolysis, nucleation and crystallization of TiO_2 precursors, and then facilitate the formation and growth of nanotubes or nanorods [25–27]. The increase of alkali concentration can offer high surface energy for curl-up of nanosheets to form nanotubes or nanorods [24,28]. The length, growth rate, and density of TiO_2 nanostructures are improved with the certain reaction time, but the length and density remained constant at higher time due to the decrease of precursor concentration [24,29,30]. Additionally, in acid washing process, H^+ replacing Na^+ ions can alter the forces in the layered titanate, decreasing the interlayer distance, which changes the surface property and morphology of material [31,32]. For instance, with H^+ concentration increased, the morphology can be transformed from lamellar structure to nanotubes or nanorods [24]. Nevertheless, to date, it still lacks a study which comprehensively investigates the effects of other hydrothermal parameters including NaOH concentration, hydrothermal time and acid washing concentration on the physicochemical property and photocatalytic activity of Ti-based TiO_2 nanomaterials. Furthermore, the growth mechanism of TiO_2 nanomaterials on Ti substrate has not been proposed.

Thus, in this study, we extended our previous study through systematical investigating the effects of critical manufacturing parameters on the physicochemical properties (including micromorphology, crystal structure, UV-light absorption and separation efficiency of photo-generated charge carriers). According to the results of micro-morphology, crystal structure, and UV-light absorption of Ti-based TiO_2 nanomaterials, the growth mechanism of TiO_2 nanomaterials on Ti substrate by the hydrothermal process was proposed. Moreover, the prepared Ti-based TiO_2 nanomaterials were used for photocatalytic degradation of endocrine disrupter BPA to optimize the hydrothermal parameters. At last, BPA degradation intermediates by TiO_2 nanomaterials prepared at optimal conditions were identified, and its degradation pathways were proposed.

Materials and methods

Materials

Sodium hydroxide (NaOH), hydrochloric acid (HCl), hydrofluoric acid (HF), nitric acid (HNO_3) and bisphenol A (BPA) were purchased from Sinopharm Chemical Reagent Co. Ltd. All chemicals were analytical grade and used without any further purification. Titanium plates (0.5 mm thickness, 99.8% purity) were obtained from Dongguan Fu Tai Metal Materials Co., Ltd. Milli-Q ultrapure water was used to prepare all solutions.

Preparation of Ti-based TiO_2 nanomaterials

Ti-based TiO_2 nanomaterials were prepared by the hydrothermal treatment of Ti plate. Prior to hydrothermal reaction, Ti plates were ultrasonically cleaned in detergent solution, acetone, ethanol and deionized water according to our previous study [21]. The purified Ti plates were then steeped into a mixture of diluted HF and HNO_3 ($HF:HNO_3:H_2O$ = 1:4:5 in volume) for 45 s, followed by washing with deionized water and drying at room temperature. Next, the pre-processed Ti plates were placed into a 50 mL para-polyphenyl-lined stainless steel autoclave, which contained 20 mL of NaOH aqueous solution and its concentration was 0.5–4 M. The sealed autoclaves were maintained in an electric oven for predetermined time (from 1 to 36 h) at scheduled temperature (from 140 to 220℃), followed by naturally cooling down to ambient temperature. After the hydrothermal procedure, Ti plates covered with nanomaterials were rinsed by deionized water for several times and immersed into HCl solution for exchanging Na^+ with H^+. The concentration of HCl solution was ranged from 0.05 to 0.3 M, and HCl washing time was kept for 24 h. Finally, the samples were calcinated in muffle furnace at 500℃ with a heating rate of 3℃/min.

Characterization of Ti-based TiO_2 nanomaterials

The morphology of the as-manufactured nanomaterials was photographed with a field emissions scanning electron microscope (FE-SEM, Hitachi S4800, Japan) at an acceleration voltage of 5 kV. The sizes of TiO_2 nanomaterials were determined quantitatively with the Nano Measurer 1.2 and the results were displayed in Figs. S1-S6. The optical absorption curves of samples were recorded on a UV–visible spectrophotometer (UV-2550, SHIMADZU) equipped with an integrating sphere detector, using $BaSO_4$ as background sample. A Rigaku D/MAX III-3B diffractometer was used to test the crystal structure of Ti-based TiO_2 nanomaterials (X-ray diffraction, XRD). The crystallite size of TiO_2 nanomaterials was calculated with the Debye-Scherrer formula [33,34]. The transient photocurrent was measured by using a CHI660E electrochemical workstation in a standard three-electrode configuration, in which Ti-based TiO_2 nanomaterials, Pt plate and saturated calomel electrode were used as the work electrode, counter electrode and reference electrode, respectively. A Na_2SO_4 solution was used as the supporting electrolyte.

Photocatalytic degradation of BPA

The photocatalytic removal of BPA was carried out in a 50 mL self-made cylindrical quartz photo-reactor filled with 30 mL of BPA (5 mg/L) aqueous solution. The photocatalyst was vertically immersed into the BPA solution and fixed in the photo-reactor, and photoreaction areas were 1×3 cm^2. A 300 W Xenon Lamp was placed 15 cm away from the photo-reactor and served as the simulated solar light with an irradiation intensity of 32.6 KLux. At regular intervals, the degraded samples were collected and injected into the vials. The concentration of BPA was detected by a High Performance Liquid Chromatography (HPLC, Waters 2998) equipped with a Waters symmetry C18 column (150×4.6 mm, 5 μm). A mixture of 35% ultrapure water (containing 0.1% acetic acid) and 65% methanol was used as the mobile phase, and its flow rate was set as 1 mL/min. The injection volume of sample was 80 μL, and the detection wavelength was set at 275 nm. The degradation intermediates of BPA were detected with a Liquid Chromatography/Mass spectroscopy (LC/MS) in a negative

electrospray ionization mode (Agilent 1260 HPLC-ABSciex QTrap 5500 MS, HPLC/ESI-QqQ). The detection parameters of LC/MS were displayed in Text S1 in the supplementary material.

Results and discussion

Effect of manufacturing parameters on the morphology of Ti-based TiO_2 nanomaterials

Fig. 1a shows SEM image of fresh Ti plate, and Fig. 1b-f display SEM images of Ti-based TiO_2 nanomaterials fabricated with different NaOH concentration under hydrothermal temperature of 180℃ and hydrothermal time of 16 h. When NaOH concentrations were 0.5 M and 1 M, Ti-based TiO_2 presented the nanosheets structure, which interlaced with each other to form porous arrays. At NaOH concentration of 0.5 M, a small amount of TiO_2 nanotubes were produced among TiO_2 nanosheets labeled by blue arrows. Increasing concentration of NaOH to 2–3 M, morphology of TiO_2 nanosheets changed obviously. The sizes of nanosheets decreased dramatically, and partial nanosheets presented tilted and/or bent, together with a small amount of nanowires were observed. Further improving NaOH concentration to 4 M, nanowires disappeared and surface layers of TiO_2 nanosheets exhibited coarse morphology and consisted of some smaller nanosheets (compared to Fig. 1b-e). The detailed nanosheets sizes were exhibited in Fig. S1 and S2. With increase of NaOH concentration from 0.5 M to 4.0 M, the width and thickness of TiO_2 nanosheets decreased from 514-2593 nm and 30–78 nm to 175–617 nm and 28–43 nm, respectively.

As indicated by previous work, hydrothermal temperature is a crucial parameter in controlling the morphology of nanomaterials [23]. Fig. 2 exhibits the morphology variation of Ti-based TiO_2 nanomaterials fabricated at different hydrothermal temperatures under identical concentration of NaOH of 1.0 M and hydrothermal time of 16 h. Clearly, TiO_2 nanobelts assemblage (compare to nanosheets' size) with high density were formed at hydrothermal temperature of 140℃. By measurement, the width

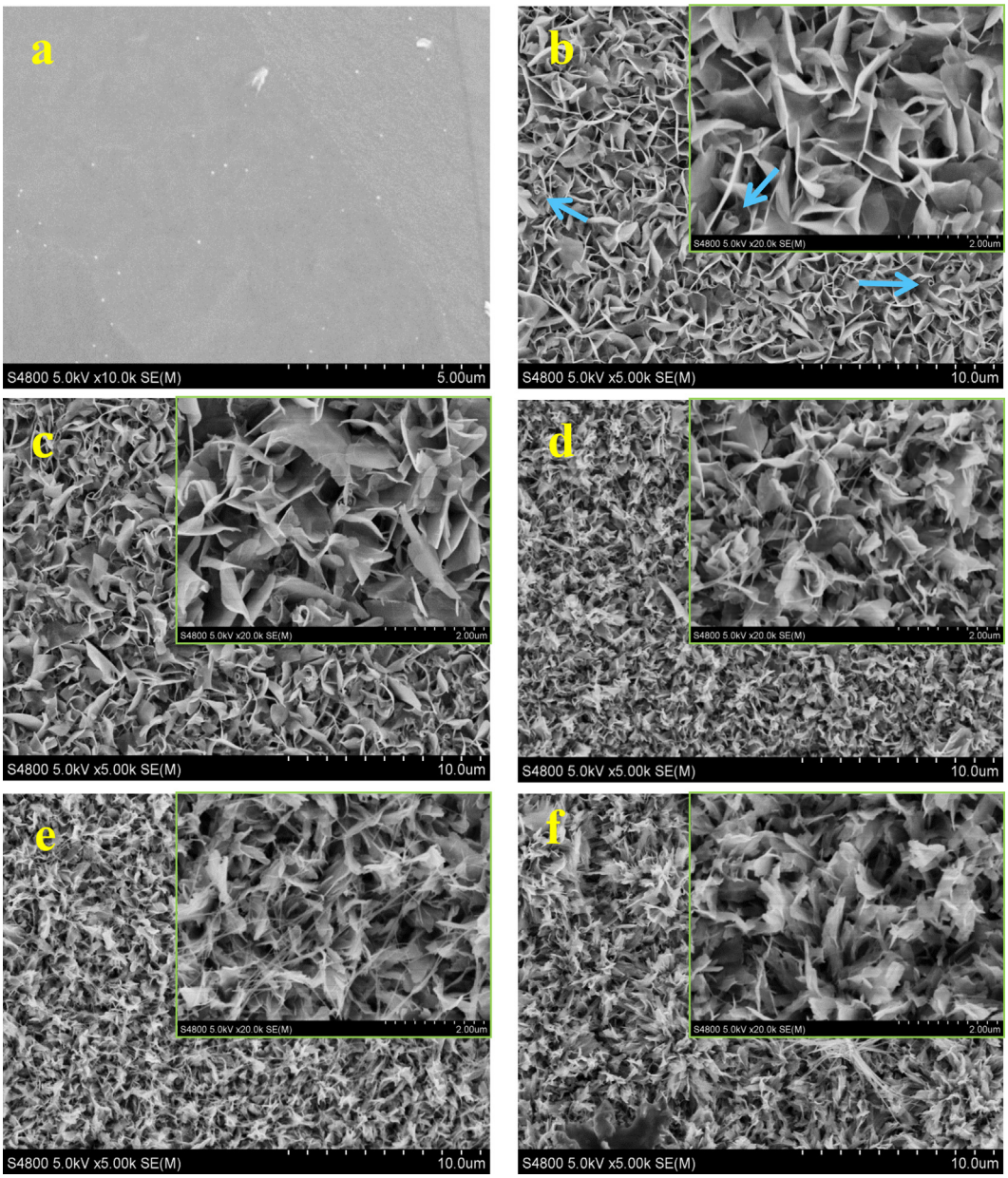

Fig. 1. SEM images of fresh Ti plate (a) and Ti-based TiO_2 nanomaterials manufactured at NaOH concentration of 0.5 M (b), 1 M (c), 2 M (d), 3 M (e) and 4 M (f).

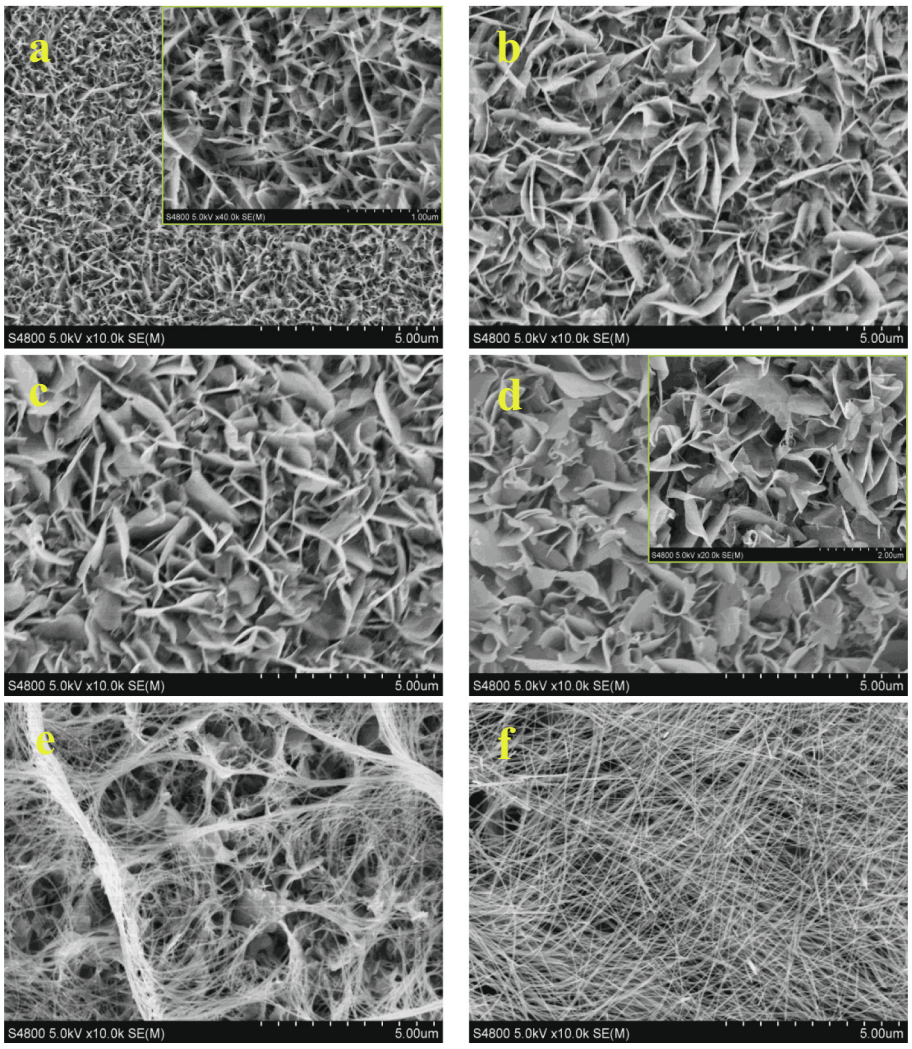

Fig. 2. SEM images of Ti-based TiO_2 nanomaterials manufactured at hydrothermal temperature of 140℃ (a), 160℃ (b), 170℃ (c), 180℃ (d), 200℃ (e) and 220℃ (f).

and thickness of nanobelts were 38–89 nm and 10–25 nm, respectively (Fig. S3 and S4). When hydrothermal temperature was up to 160-180℃, morphology of TiO_2 nanomaterials obviously changed. At 160℃, surface of Ti-based TiO_2 was composed almost exclusively of uneven size nanosheets (width of 305–1939 nm and thickness of 19–73 nm), while relatively ordered nanosheets were formed at 170℃ (width of 448–2236 nm and thickness of 20–75 nm). Furthermore, nanosheets with width of 434–2438 nm and thickness of 21–74 nm were formed and partial nanosheets presented incline posture at 180℃. Increasing temperature to 200℃, transformation of outer nanosheets to nanowires was observed, with thickness of 23–62 nm. With further increasing temperature to 220℃, the underlying nanosheets disappeared and superficial morphology was composed of intertwined nanowires of 22–63 nm thickness [23].

Fig. 3 shows SEM images of TiO_2 nanomaterials prepared at hydrothermal temperature of 170℃ and concentration of NaOH of 1.0 M for different hydrothermal time. At hydrothermal reaction of 1 h, high-density nanobelts in a width of 22–86 nm and a thickness of 7–19 nm were formed on the surface of Ti-based TiO_2 (Fig. S5 and S6). After 3 h reaction, surface of Ti-based TiO_2 was covered by nanobelts accompanied with some nanosheets, in which nanobelts showed the width of 25–93 nm and thickness of 6–20 nm, and the width and thickness of nanosheets were 150–488 nm and 14–26 nm, respectively. When hydrothermal time was increased to 6 h, the number of nanobelts decreased and its width decreased from 25-93 nm to 20–59 nm. Meanwhile, the number of nanosheets increased and its width increased to 327–1203 nm, while the thickness remained unchanged (13–26 nm). When hydrothermal time was 12 h, nanobelts almost completely disappeared, and porous arrays consisted of nanosheets with the width of 419–1458 nm and thickness of 17–30 nm were covered on the surface of Ti substrate. However, with further increasing hydrothermal time to 16–36 h (Fig. 3e-j), all the hydrothermal products on the surface of Ti substrate were made up of nanosheets without any other morphologies, and its width and thickness had no obvious change (Fig. S5 and S6).

Usually, acid washing procedure is a critical process after alkaline hydrothermal reaction [24,35]. Therefore, we varied concentration of HCl in the range of 0.05–0.3 M to investigate its effect on the morphology of TiO_2 nanosheets (Fig. 4), which were fabricated at NaOH concentration of 1 M, hydrothermal temperature of 170 ℃ and hydrothermal time of 28 h. When HCl concentration was lower than 0.1 M, the dense nanosheets with perfect morphology could be clearly observed in Fig. 4. The surface of Ti-based TiO_2 nanomaterials presented the sparse and large-sized nanosheets after acid washing in 0.2 M HCl solution, implying that flake-like structure of TiO_2 was distinctly corroded (Fig. 4c). Further increase of HCl concentration corroded more TiO_2 nanosheets apparently

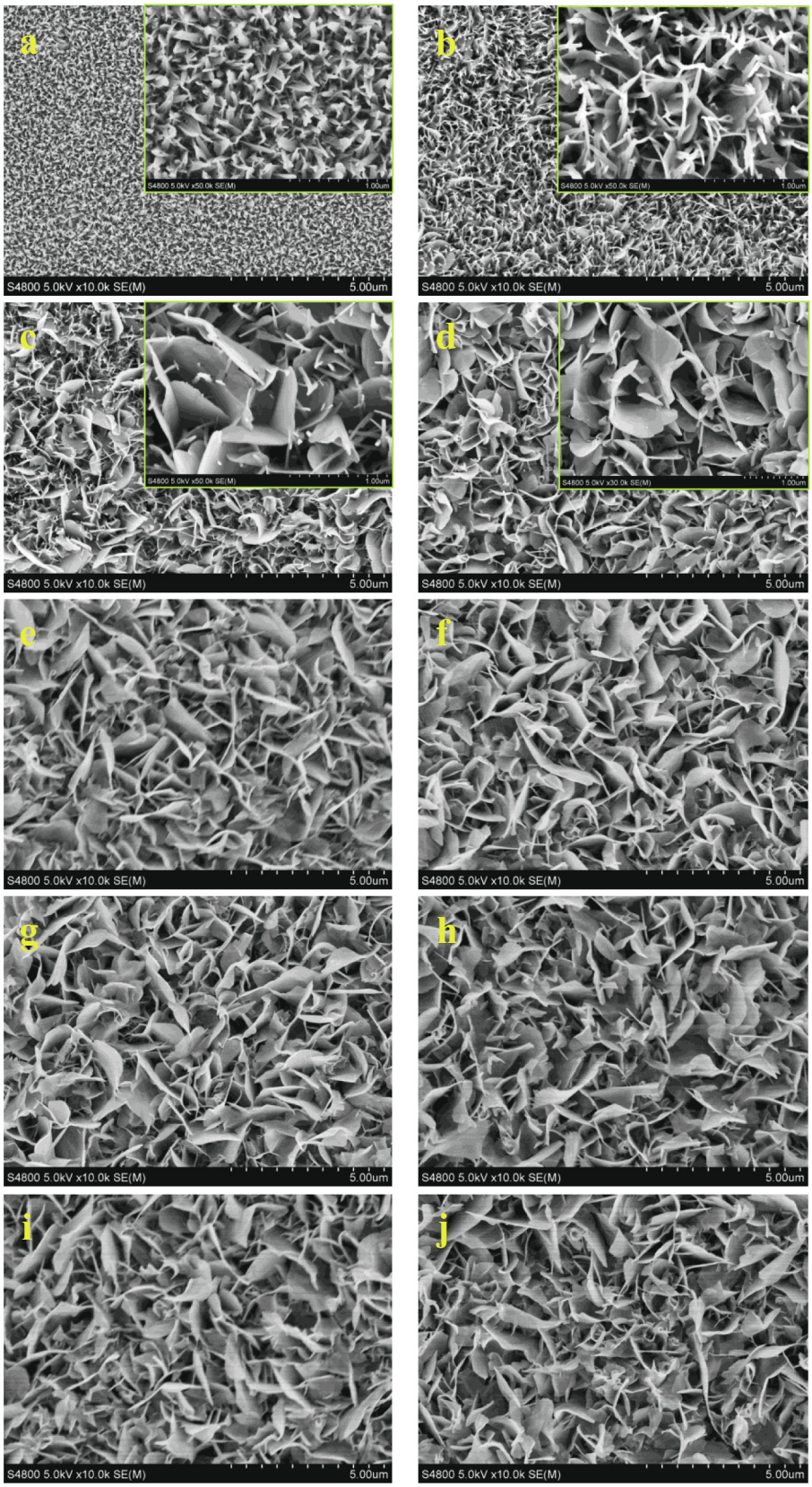

Fig. 3. SEM images of Ti-based TiO_2 nanomaterials manufactured at hydrothermal time of 1 h (a), 3 h (b), 6 h (c), 12 h (d), 16 h (e) 20 h (f), 24 h (g), 28 (h), 32 h (i), and 36 h (j).

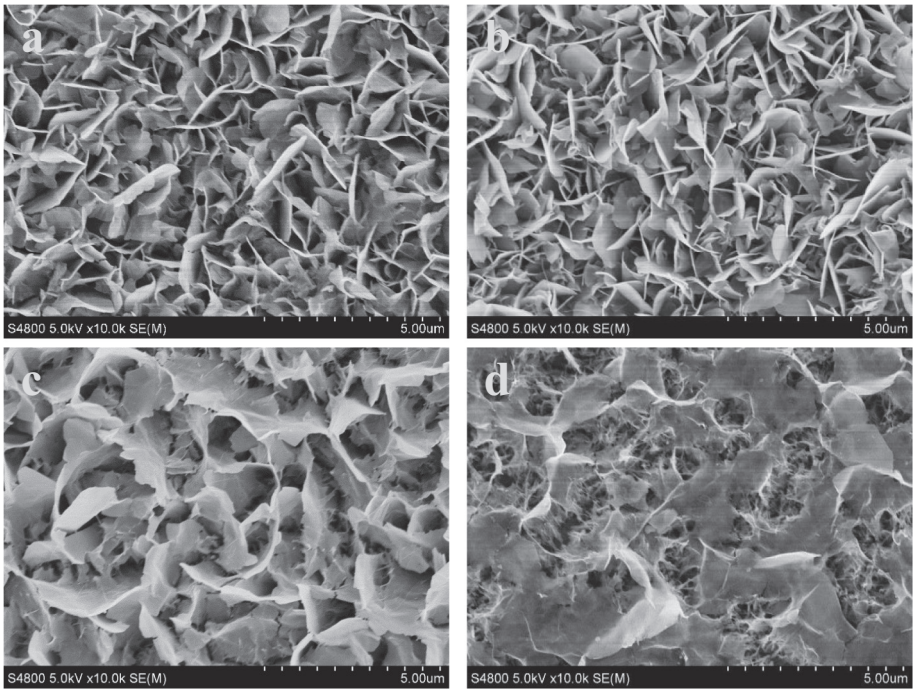

Fig. 4. SEM images of Ti-based TiO_2 nanomaterials washed with HCl concentration of 0.05 M (a), 0.1 M (b), 0.2 M (c) and 0.3 M (d).

(Fig. 4d). The change of surface morphology would influence the photocatalytic activity of Ti-based TiO_2 nanosheets.

Effect of manufacturing parameters on the crystal structure of Ti-based TiO_2 nanomaterials

Fig. 5 exhibits XRD patterns of Ti-based TiO_2 nanomaterials at different manufacturing parameters. The characteristic diffraction peaks at 25.3° and 27.4° were anatase TiO_2 (101 plane) and rutile TiO_2 (110 plane) [34], respectively, and the strong diffraction peaks at 40.1°, 53.0°, and 70.6° were assigned to Ti metal phase (JCPDS NO. 44–1294). As increase of NaOH concentration, hydrothermal temperature and hydrothermal time, all the intensity of anatase TiO_2 (101) plane improved gradually, while the peak intensity of rutile TiO_2 (110) plane did not increase significantly, and even decreased at some conditions (high concentration of NaOH). Thus, the intensity ratio of the ($I_{(101)}/I_{(110)}$) crystal planes increased (Table S1-S4) with increase of NaOH concentration, temperature and time, which indicated that more TiO_2 grew on (101) crystal plane on Ti substrate, and there was no correlation between $I_{(101)/I(110)}$ ratio and morphological variation. Furthermore, in Fig. 5c, there were no TiO_2 signal at 1 h of reaction, which might be attributed to the fact that TiO_2 content was too little to be detected by XRD. And further improving reaction time more than 28 h resulted in a slight decrease of peak intensity, but did not influence $I_{(101)}/I_{(110)}$ ratio. The decrease of peak intensity indicated that TiO_2 nanomaterials was no longer growth, and some even dissolved [21].

The crystallite size of anatase TiO_2 was calculated and shown in Table S1-S4. The increase of NaOH concentration did not affect crystallite size of anatase TiO_2. Nevertheless, with increase of hydrothermal temperature, crystallite size of anatase TiO_2 first increased and then decreased (>200℃). Additionally, crystallite size increased steadily with the reaction time (<16–20 h), while changed a little when reaction time exceeded 16–20 h. The crystallite size was obvious correlation with morphology. TiO_2 nanosheets exhibited a big crystallite size in the range of 15.6–20.2 nm, and TiO_2 nanobelts and TiO_2 nanowires presented the small crystalline size of 9.5–14.9 nm and 11.2 nm, respectively. The HCl washing procedure (replacing Na^+ with H^+) also affected the crystal structure of TiO_2 [24]. The characteristic peaks intensities of anatase TiO_2 and rutile TiO_2 at 0.05 M HCl were identical to that of 0.1 M HCl, but a slight smaller diffraction angle was obtained at 0.1 M HCl (Fig. 5e), which meant that a smaller crystallite size of TiO_2 was formed at 0.1 M HCl (Table S4). The high concentration of HCl would corrode TiO_2 nanosheets, and lower its characteristic peak and the $I_{(101)}/I_{(110)}$ ratio, together with crystallite size (Table S4), which was in accordance with SEM results (Fig. 4).

Effect of manufacturing parameters on the optical property of Ti-based TiO_2 nanomaterials

The UV–vis diffuse reflectance spectra of Ti-based TiO_2 nanomaterials at different manufacturing parameters were shown in Fig. 6. All the samples exhibited intrinsic absorption of UV-light region. Besides, all the samples showed a broad visible-light (400–850 nm) absorption, possibly caused by the following aspects including absorption of incident light by the nanosheets/nano belts/nanowires, trapped charge carriers, or some colored centers, which was consistent with previous reports [36,37]. At different concentration of NaOH, TiO_2 nanomaterials with high anatase crystallinity and well crystal structure exhibited the improved UV-light absorption. However, this phenomenon was opposite to the results of different hydrothermal temperature and hydrothermal time (High anatase crystallinity and well crystal structure displayed the low UV-light absorbance). This indicated that crystallinity and crystal structure of TiO_2 nanomaterials did not well correlate with UV-light absorption in this study. The variation of UV-light absorbance might be mainly influenced by the morphology of nanomaterials.

With increase of NaOH concentration, UV-light absorbance of TiO_2 nanosheets increased (Fig. 6a), which was mainly related to decrease of the nanosheets size (Table S1 and S2). At different

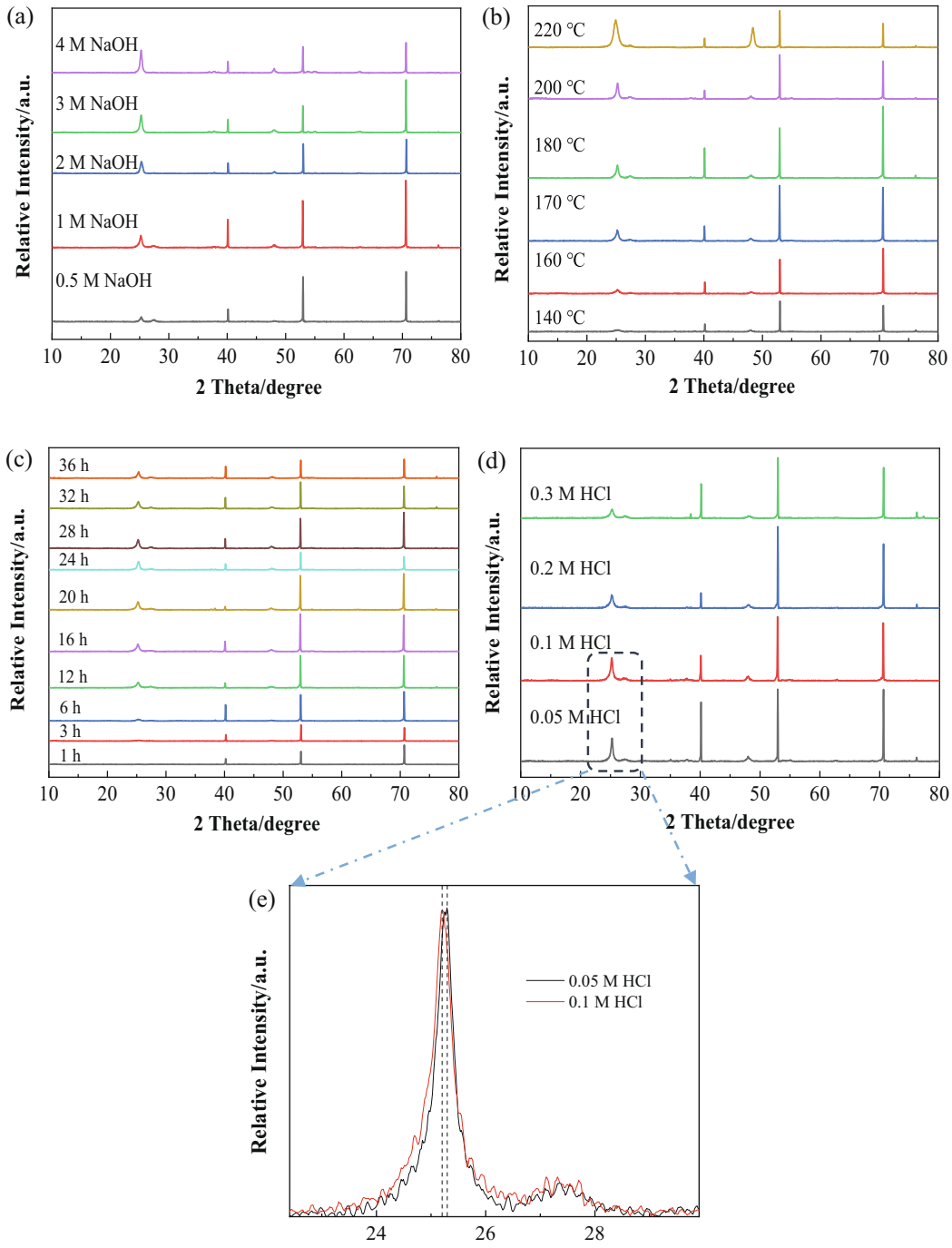

Fig. 5. XRD patterns of Ti-based TiO_2 nanomaterials manufactured at different NaOH concentration (a), hydrothermal temperature (b), hydrothermal time (c), HCl washing concentration (d, e).

hydrothermal temperature, UV-light absorbance of TiO_2 nanomaterials with different morphology was arranged in order of TiO_2 nanobelts > TiO_2 nanosheets > TiO_2 nanowires (Fig. 6b). The smaller size of nanobelts and/or nanosheets might absorb more UV-light. The intertwined nanowires would block the effective absorption of UV-light. Furthermore, influence of hydrothermal time on UV-light absorbance of TiO_2 nanomaterials also conformed to the change of morphology, that is, with increase of hydrothermal time, TiO_2 nanobelts gradually transformed into TiO_2 nanosheets (Fig. 3), and nanobelts showed a stronger UV-light absorbance than that of nanosheets (Fig. 6c). As hydrothermal time increased from 16 h to 36 h, UV-light absorbance of TiO_2 nanosheets hardly changed, which corresponded well to the SEM results (The morphology did not change significantly). In Fig. 6d, HCl washing concentration had a great influence on the UV-light absorbance. The UV-light absorbance of TiO_2 nanomaterials gradually decreased with increasing HCl concentration, which was due to the destruction of nanosheets morphology.

The plots of $(\alpha h\nu)^{1/2}$ versus $h\nu$ were displayed in Fig. S7 and energy gap (Eg) values of TiO_2 nanomaterials with various morphologies were given [38–40]. The theoretical Eg values of anatase TiO_2 and rutile TiO_2 are 3.2 eV and 3.0 eV, respectively. The pre-

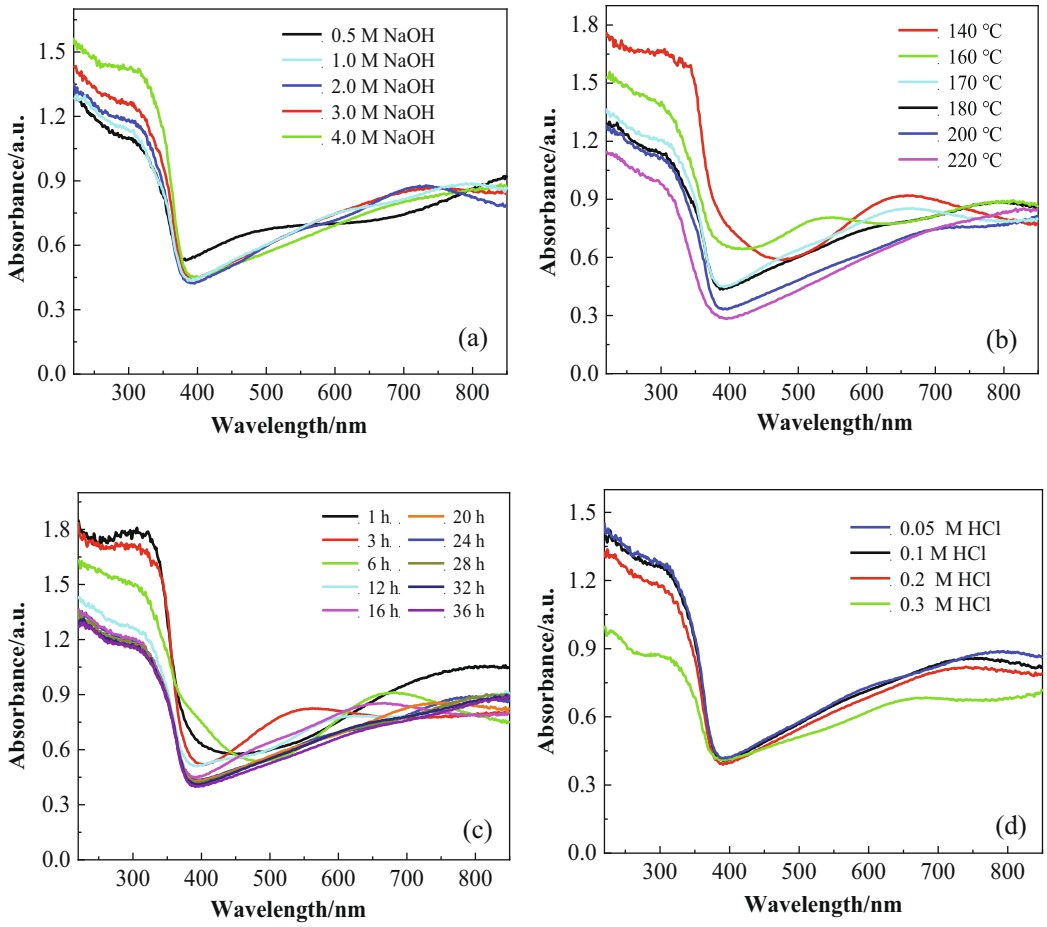

Fig. 6. UV–Vis diffuse reflectance spectra of Ti-based TiO_2 nanomaterials manufactured at different NaOH concentration (a), hydrothermal temperature (b), hydrothermal time (c), and HCl washing concentration (d).

pared TiO_2 nanomaterials revealed a mixed crystal structure, thus most of Eg values were in the range of 3.04–3.19 eV. It should be noted that TiO_2 nanosheets accompanied with a small amount of nanobelts (or nanosheets in smaller sizes) revealed a small Eg value (2.88 eV and 2.86 eV for the samples of Fig. 2b and Fig. 3c, respectively), indicating that this morphology could respond to visible light. Bade et al. [41] synthesized highly dense and lengthy TiO_2 nanorods with a band gap of 2.8–2.9 eV, which could be also activated by visible light. However, detailed reasons required further investigation.

Growth mechanism of TiO_2 nanomaterials

Based on the above results, the formation mechanism of TiO_2 nanomaterials on Ti substrate by hydrothermal process was proposed as follows (Fig. 7). In NaOH solution, sodium titanate nanocrystals as the crystal nucleus were first formed on Ti plate surface in the primary hydrothermal stage. Then, nano-materials began to grow on sodium titanate nanocrystals. Meanwhile, Ti atoms on the surface of Ti plate gradually dissolved, and diffused to the surface of crystal nucleus for crystallization (mainly on (101) plane). This dissolution-crystallization process was directly related to the different NaOH concentration, hydrothermal temperature, and hydrothermal time. The higher NaOH concentration with more Na^+ ions would lead to a faster Ti dissolution, and also a faster and a more disorderly crystal of sodium titanate, which increased the crystal intensity of anatase TiO_2 and promoted the transformation from relative ordered nanosheets to coarse and crooked nanosheets [24,28]. Furthermore, both the dissolution speed of Ti substrate and crystallization speed of sodium titanate gradually increased with boosting the hydrothermal temperature. Thus, the crystal intensity of anatase TiO_2 steadily enhanced, and TiO_2 nanobelts gradually grew into the nanosheets (<180℃). However, when hydrothermal temperature surpassed 180℃, the direction of crystallization nucleation of sodium titanate might be changed or the formed sodium titanate might undergo a "nucleation-dissolution–recrystallization" process [42,43], therefore generating nanowires. As increase of hydrothermal time, sodium titanate nanocrystals firstly grew into nanobelts. Then some of nanobelts gradually dissolved, and redeposited on other nanobelts crystals to grow into nanosheets. This process could be also explained by "nucleation-dissolution–recrystallization" growth mechanism of Ostwald ripening [42,43]. This was the reason that width of TiO_2 nanobelts decreased gradually with increase of hydrothermal time (Fig. S5). After a certain time, dissolution of Ti substrate or sodium titanate crystal and crystallization of sodium titanate would achieve a dynamic equilibrium, so nanosheets did not grow.

Effect of manufacturing parameters on the photoelectrochemical property of Ti-based TiO_2 nanomaterials

The photoelectrochemical measurement was considered as an efficient approach to analyze the separation efficiency of photo-

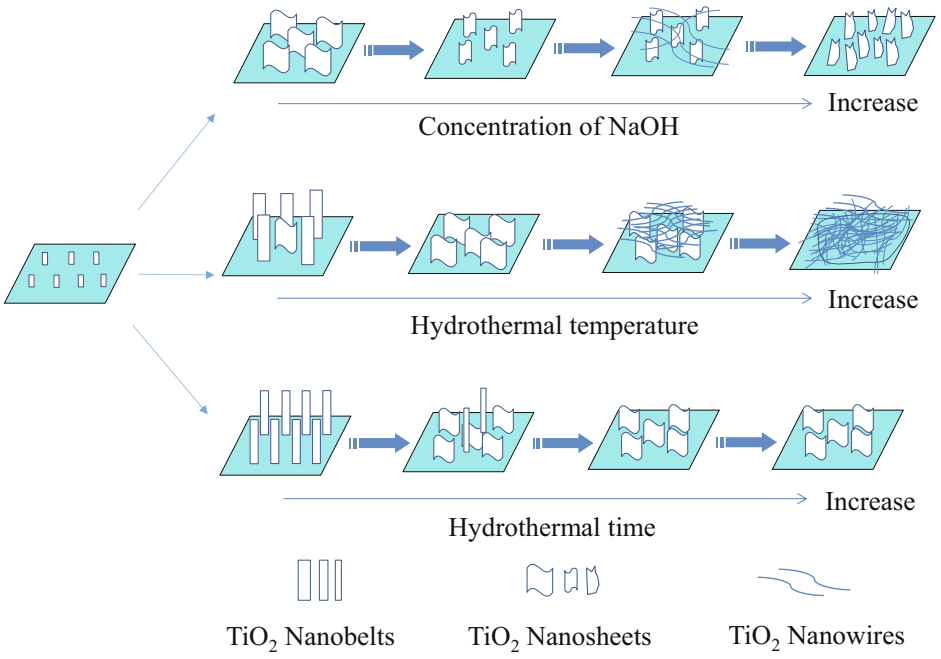

Fig. 7. Growth mechanism diagram of TiO_2 nanomaterials.

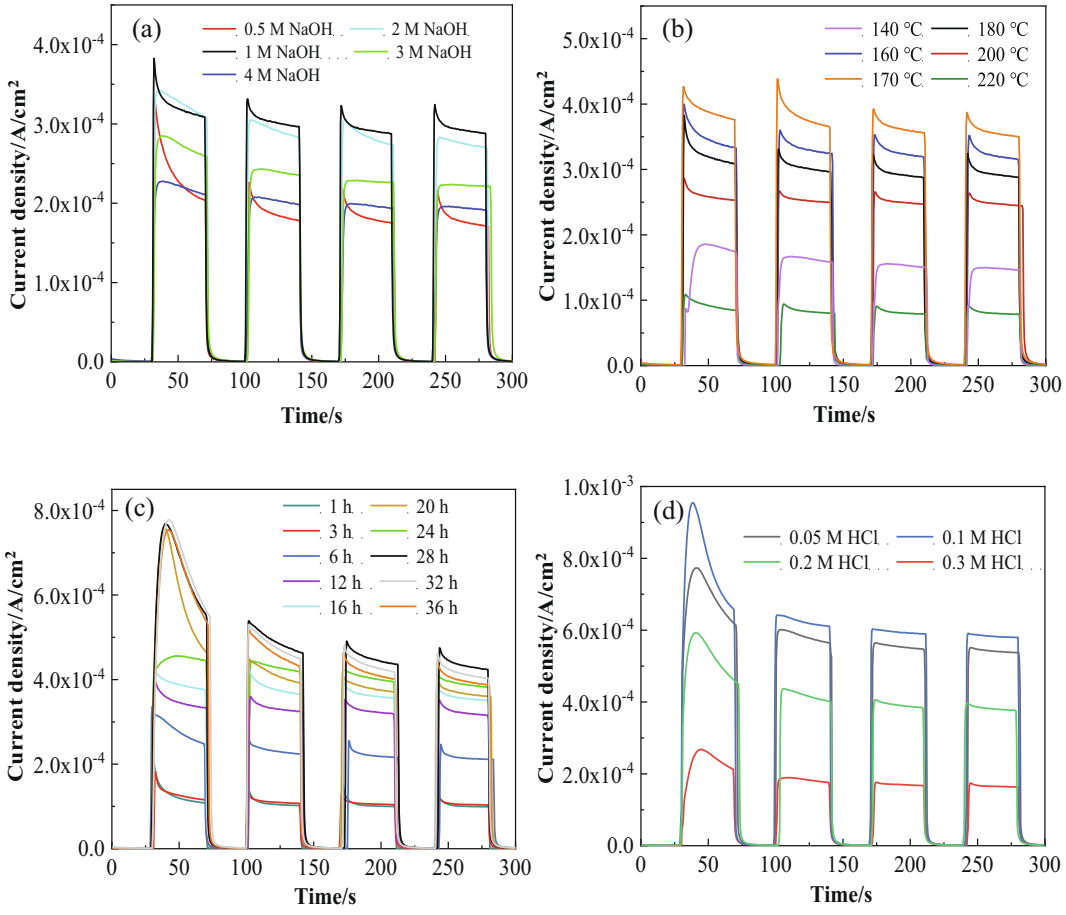

Fig. 8. Transient photocurrent response of Ti-based TiO_2 nanomaterials manufactured at different NaOH concentration (a), hydrothermal temperature (b), hydrothermal time (c), and HCl washing concentration (d).

generated charge carriers, which was an important index to evaluate the photocatalytic property [44,45]. Fig. 8 displays the transient photocurrent response of Ti-based TiO_2 nanomaterials in a number of on–off cycles of light irradiation. As increasing concentration of NaOH (Fig. 8a), transient photocurrent of Ti-based TiO_2 first improved and then declined, and Ti-based TiO_2 nanosheets manu-

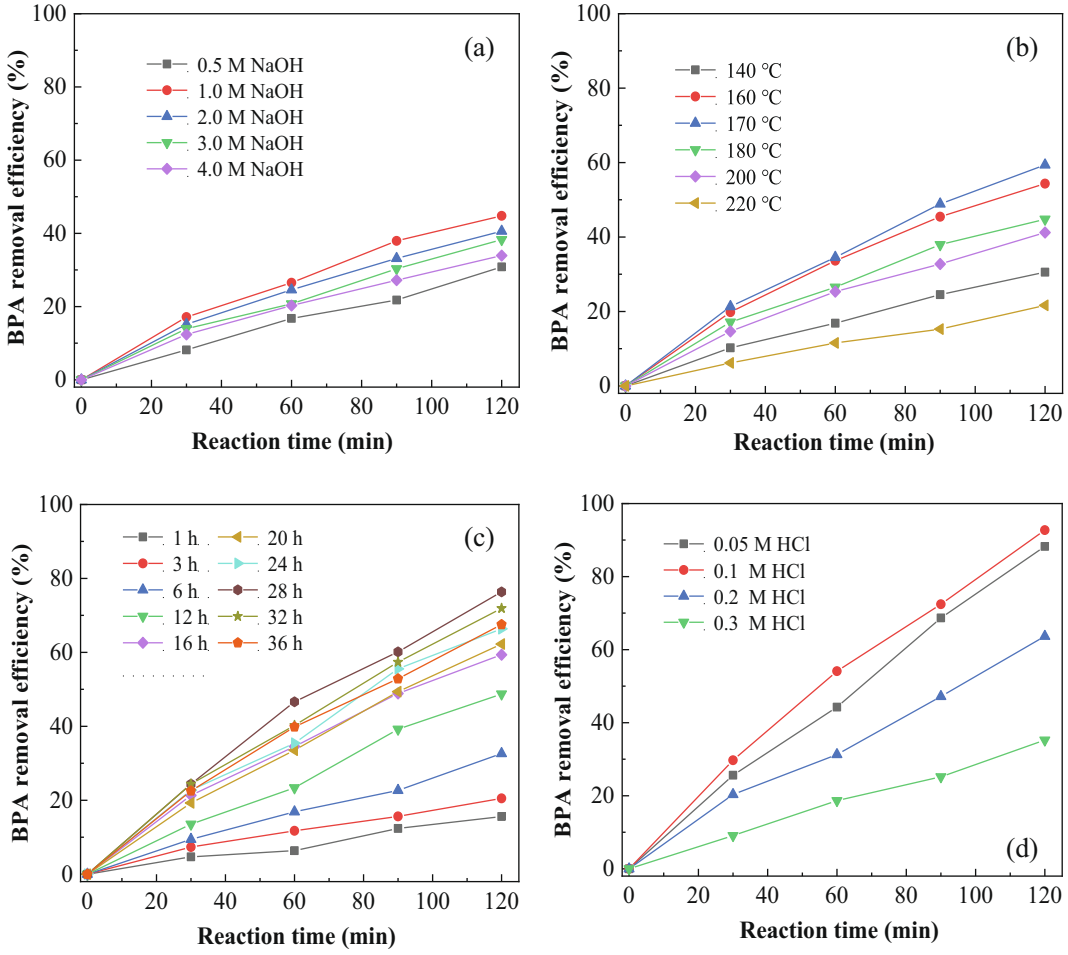

Fig. 9. Effect of manufacturing parameters on photocatalytic degradation of BPA over the Ti-based TiO_2 nanomaterials: (a) concentration of NaOH, (b) hydrothermal temperature, (c) hydrothermal time, (d) concentration of HCl. Conditions: [BPA] = 5 mg/L, Volume = 30 mL, pH = 6.4, T = 25℃±1℃.

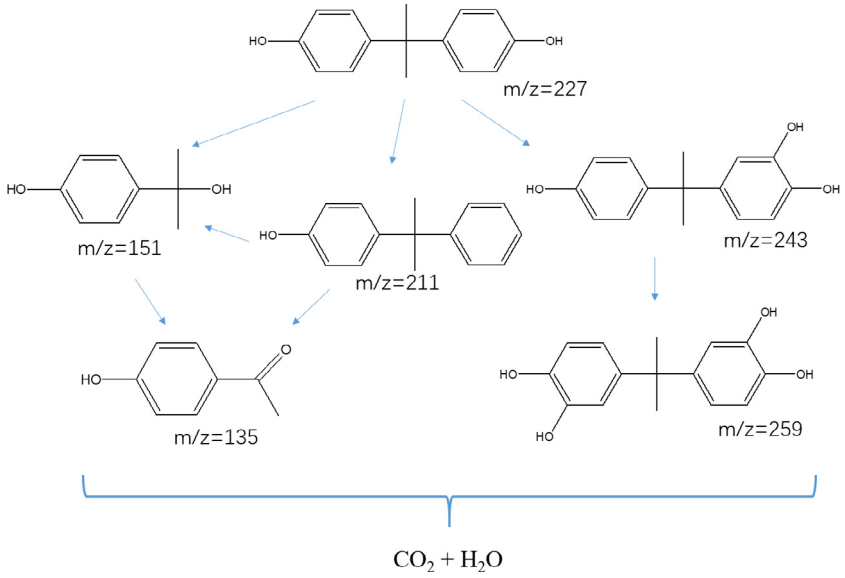

Fig. 10. Possible degradation pathways of BPA by Ti-based TiO_2 nanosheets at the optimal prepared parameter. Conditions: [BPA] = 5 mg/L, Volume = 30 mL, pH = 6.4, T = 25℃±1℃.

factured at 1 M NaOH showed the highest photoinduced current, indicating the highest separation efficiency of photogenerated electron-hole pairs. Although the crystal intensity and UV-light absorbance of Ti-based TiO_2 were not the highest at NaOH concentration of 1.0 M, the highest photocurrent might be a comprehensive result of crystal structure, light absorption and morphology. For the hydrothermal temperature, the photoinduced current might be mainly affected by the material morphology. As shown in Fig. 8b, TiO_2 nanosheets would exhibit a higher separation efficiency of photoinduced electron-hole pairs than that of TiO_2 nanobelts and TiO_2 nanowires. The nanosheets structure was beneficial to establish straight electronic transmission paths to facilitate the carrier transport [46]. Among the three TiO_2 nanosheets prepared at 160℃, 170℃, and 180℃, TiO_2 nanosheets prepared at 170℃ presented a highly ordered nano-lamellar structure, thus resulting in a high photogenerated current. The effect of hydrothermal time on the photogenerated current was shown in Fig. 8c. The photogenerated current of Ti-based TiO_2 nanomaterials enhanced steadily with hydrothermal time, and the highest photocurrent was achieved at 28 h of reaction. Further boosting hydrothermal time lowered the photocurrent. This was attributed to the fact that highly ordered nanosheets were gradually formed and crystal intensity was improved with the reaction time (from 1 h to 28 h), while further increasing time (>28 h) would decrease the peak intensity (or crystallinity) of anatase TiO_2 (Fig. 5c). The HCl washing concentration also greatly affected the photocurrent of TiO_2 nanosheets (Fig. 8d). TiO_2 nanosheets washed with 0.1 M HCl showed a slightly higher photocurrent than that of 0.05 M HCl washed TiO_2 nanosheets, which might be due to the fact that a small crystallite size was favorable for the separation of photoinduced electrons and holes. The low photocurrent of TiO_2 nanosheets treated by high concentration of HCl would be ascribed to the destruction of morphology and crystal structure.

Effect of manufacturing parameters on the photocatalytic activity of Ti-based TiO_2 nanomaterials

The photocatalytic performances of Ti-based TiO_2 nanomaterials were evaluated by the degradation of BPA. The removal rate of BPA from direct photolysis within 120 min was less than 5%, which was much lower than that of the photocatalytic degradation processes. Fig. 9a displays that photocatalytic degradation of BPA by TiO_2 nanomaterials prepared at different concentration of NaOH. When concentration of NaOH was increased to 1 M, TiO_2 nanosheets revealed the highest photocatalytic activity, for which 44.8% of BPA was removed. As increase of NaOH concentration, the photocatalytic activity lowered gradually. Observed from Fig. 9b, when hydrothermal temperature was 170℃, TiO_2 nanosheets displayed superior photocatalytic activity for degradation of BPA (59.4%). On the contrary, lower or higher hydrothermal temperature could both reduce BPA removal. Hydrothermal time also displayed a dramatically effect for degradation of BPA (Fig. 9c). With increase of hydrothermal time, TiO_2 nanomaterials exhibited an enhanced photocatalytic activity. When hydrothermal time was 28 h, Ti-based TiO_2 nanosheets performed the highest photocatalytic degradation of BPA (76.3%). As further increase of hydrothermal time, the photocatalytic activity declined slightly. In addition, HCl washing concentration significantly influenced the photocatalytic degradation of BPA (Fig. 9d). The 0.1 M HCl washed sample possessed the best BPA removal efficiency. Hence, in this study, the optimized concentration of NaOH, hydrothermal temperature, hydrothermal time, and HCl washing concentration were 1 M, 170 ℃, 28 h, and 0.1 M, respectively. Under the optimal parameters, TiO_2 nanosheets exhibited the best photocatalytic activity, in which 92.7% of BPA could be degraded from the aqueous solution after 2 h irradiation. The photocatalytic degradation of BPA of Ti-based TiO_2 nanomaterials followed the same tendency with the photoelectrochemical property. The high photocatalytic activity of Ti-based TiO_2 nanosheets prepared at the optimal hydrothermal parameters was attributable to the relatively uniform and regular nanosheet micro-structure, well crystal structure and appropriate UV-light absorption, which was in favor of generation and separation of photo-induced charge carriers, resulting in an enhanced photocatalytic activity.

The multiple photocatalytic degradation cycles were performed to investigate the stability of TiO_2 nanosheets layer. As shown in Fig S8, BPA removal efficiency of Ti-based TiO_2 nanosheets prepared at optimal conditions decreased by approximately 5% (from 92.7% to 87.5%) after seven cycles, and the corresponding SEM image indicated that the ordered TiO_2 nanosheets layer still maintained. The results implied that TiO_2 nanosheets grown on Ti substrate exhibited good stability.

The possible degradation intermediates of BPA by Ti-based TiO_2 nanosheets at optimal parameters were listed in Fig. S9 and Table S5, and the removal pathways of BPA were proposed in Fig. 10. The identification of degradation intermediate was based on the molecular ion mass and its calibration was less than ± 0.5 Da (Table S5). Apart from the parent compound (BPA, m/z 227), five degradation intermediates were identified. First, BPA could be hydroxylated by the hydroxyl radicals to convert to molecular ion of m/z 243, and further transformed into the di-hydroxylated derivative of BPA (m/z of 259). The product of m/z = 211 probably derived from the destruction of C–O bond of BPA by reactive oxidants. Then, the electron-rich alkyl carbon could be attacked by reactive oxidants to generate intermediate of m/z 151, which was then oxidized into compound of m/z 135. Finally, some of intermediates could be mineralized into CO_2 and H_2O.

Conclusions

In summary, the hydrothermal manufacturing parameters that influence the morphology, crystal structure, light absorption, transient photocurrent and photocatalytic activity of Ti plate supported TiO_2 nanomaterials were investigated in detail. The growth process of TiO_2 nanomaterials on Ti plate followed well the Ostwald ripening mechanism. According to the photocatalytic degradation efficiency of BPA, the optimal manufacturing parameters of NaOH concentration, hydrothermal temperature, hydrothermal time, and HCl washing concentration were 1 M, 170 ℃, 28 h, and 0.1 M, respectively. Under the optimal condition, Ti-based TiO_2 nanosheets could remove 92.7% of BPA, which was ascribed to highly ordered nanosheet structure, well crystallinity, appropriate UV-light absorption, and high separation efficiency of charge carriers. The results in this work would provide useful information to tune physicochemical property of Ti-based TiO_2 nanomaterials for photocatalytic water remediation and other applications. Future attention should be focused on adding surfactant into NaOH solution to control the growth direction and crystal structure of TiO_2 nanomaterials.

Declaration of Competing Interest

The authors declare that they have no known competing financial interests or personal relationships that could have appeared to influence the work reported in this paper.

Acknowledgments

This work was supported by the Startup Foundation for Introducing Talent of Nanjing University of Information Science and Technology.

Appendix A. Supplementary data

Supplementary data to this article can be found online at https://doi.org/10.1016/j.jiec.2022.01.032.

References

[1] A. Fujishima, K. Honda, Nature 238 (1972) 37–38.
[2] M. Wang, J. Ioccozia, L. Sun, C. Lin, Z. Lin, Energy Environ. Sci. 7 (2014) 2182–2202.
[3] D. Awfa, M. Ateia, M. Fujii, M.S. Johnson, C. Yoshimura, Water Res. 142 (2018) 26–45.
[4] Z. Xiu, M. Guo, T. Zhao, K. Pan, Z. Xing, Z. Li, W. Zhou, Chem. Eng. J. 382 (2020).
[5] Z. Rao, G. Lu, A. Mahmood, G. Shi, X. Xie, J. Sun, Appl. Catal. B: Environ. 284 (2021).
[6] S.A. Zikalala, A.T. Kuvarega, H. Madhav, B.B. Mamba, S.D. Mhlanga, E.N. Nxumalo, Appl. Catal. A: Gen. 604 (2020).
[7] D. Li, X. Zhang, W. Zhang, Chem. Eng. J. 405 (2021).
[8] M. Fallah, M.-R. Zamani-Meymian, R. Rahimi, M. Rabbani, Appl. Surf. Sci. 316 (2014) 456–462.
[9] J. Jia, D. Li, X. Cheng, J. Wan, X. Yu, Appl. Catal. A: Gen. 525 (2016) 128–136.
[10] D. Ragazzon, M.H. Farstad, A. Schaefer, L.E. Walle, P. Uvdal, A. Borg, A. Sandell, Surf. Sci. 633 (2015) 102–108.
[11] D. Li, X. Cheng, X. Yu, Z. Xing, Chem. Eng. J. 279 (2015) 994–1003.
[12] J. Jia, D. Liu, S. Wang, H. Li, J. Ni, X. Li, J. Tian, Q. Wang, Sep. Purif. Technol. 253 (2020).
[13] M.R. Zamani Meymian, R. Haji Abdolvahab, A. Kosari Mehr, Appl. Surf. Sci. 480 (2019) 593–600.
[14] C. Adán, J. Marugán, E. Sánchez, C. Pablos, R. van Grieken, Electrochim. Acta 191 (2016) 521–529.
[15] X. Feng, K. Shankar, O.K. Varghese, M. Paulose, T.J. Latempa, C.A. Grimes, Nano Lett. 8 (2008) 3781–3786.
[16] X. Li, J. Zhao, S. Sun, L. Huang, Z. Qiu, P. Dong, Y. Zhang, Electrochim. Acta 211 (2016) 395–403.
[17] P. Roy, S. Berger, P. Schmuki, Angew. Chem. Int. Ed. 50 (2011) 2904–2939.
[18] B. Ma, S. Xin, Y. Xin, X. Ma, C. Zhang, M. Gao, J. Environ. Chem. Eng. 9 (2021).
[19] Q. Chen, S. Wu, Y. Xin, Chem. Eng. J. 302 (2016) 377–387.
[20] Y.J. Hwang, S. Yang, H. Lee, Appl. Catal. B: Environ. 204 (2017) 209–215.
[21] D. Li, Z. Xing, X. Yu, X. Cheng, Electrochim. Acta 170 (2015) 182–190.
[22] C. Wang, X. Zhang, Y. Zhang, Y. Jia, J. Yang, P. Sun, Y. Liu, J. Phys. Chem. C 115 (2011) 22276–22285.
[23] D. Li, X. Yu, X. Cheng, Funct. Mater. Lett. 08 (2014) 1550034.
[24] T. Gupta, Samriti, J. Cho, J. Prakash, Mater. Today Chem. 20 (2021).
[25] R. Hidayat, G. Fadillah, S. Wahyuningsih, I.O.P. Conf, Ser. Mater. Sci. Eng. 578 (2019).
[26] Y. Lan, X.P. Gao, H.Y. Zhu, Z.F. Zheng, T.Y. Yan, F. Wu, S.P. Ringer, D.Y. Song, Funct, . Mater. 15 (2005) 1310–1318.
[27] N. Liu, X. Chen, J. Zhang, J.W. Schwank, Catal. Today 225 (2014) 34–51.
[28] S. Sreekantan, L.C. Wei, J. Alloy. Compd. 490 (2010) 436–442.
[29] A. Ranjitha, N. Muthukumarasamy, M. Thambidurai, D. Velauthapillai, S. Agilan, R. Balasundaraprabhu, Optik 126 (2015) 2491-2494.
[30] Y. Zhao, X. Gu, Y. Qiang, Thin Solid Films 520 (2012) 2814–2818.
[31] J. Xiong, L. He, J. Exp. Nanosci. 12 (2017) 384–393.
[32] J.N. Nian, H. Teng, J. Phys. Chem. B 110 (2006) 4193–4198.
[33] S.A. Zikalala, A.T. Kuvarega, B.B. Mamba, S.D. Mhlanga, E.N. Nxumalo, Mater. Today Chem. 10 (2018) 1–18.
[34] J. Jia, D. Li, J. Wan, X. Yu, J. Ind. Eng. Chem. 33 (2016) 162–169.
[35] X. Zhang, D. Li, J. Wan, X. Yu, Mater. Sci. Semicond. Process. 43 (2016) 47–54.
[36] D. Li, J. Jia, T. Zheng, X. Cheng, X. Yu, Appl. Catal. B: Environ. 188 (2016) 259–271.
[37] X. Ma, Q. Chen, G. Liu, Y. Zhou, D. Ma, S. Xin, C. Yu, B. Zhang, Y. Xin, Chem. Eng. Sci. 226 (2020).
[38] P. Calandra, A. Ruggirello, A. Pistone, V. Turco Liveri, J. Clust. Sci. 21 (2010) 767–778.
[39] P. Calandra, D. Lombardo, A. Pistone, V. Turco Liveri, S. Trusso, J. Nanopart. Res. 13 (2011) 5833–5839.
[40] S.A. Zikalala, R. Selvaraj, F.A. Marzouqi, A.T. Kuvarega, B.B. Mamba, S.D. Mhlanga, E.N. Nxumalo, J. Environ. Chem. Eng. 8 (2020) 104082.
[41] B.R. Bade, S. Rondiya, S.R. Bhopale, N.Y. Dzade, M.M. Kamble, A. Rokade, M.P. Nasane, M.A. More, S.R. Jadkar, A.M. Funde, SN Appl. Sci. 1 (2019) 1073.
[42] F. Shao, J. Sun, L. Gao, S. Yang, J. Luo, J. Phys. Chem. C 115 (2011) 1819–1823.
[43] L. Chen, Y. Zhou, H. Dai, Z. Li, T. Yu, J. Liu, Z. Zou, J. Mater. Chem. A 1 (2013) 11790–11794.
[44] R. Montenegro-Ayo, A.C. Barrios, I. Mondal, K. Bhagat, J.C. Morales-Gomero, M. Abbaszadegan, P. Westerhoff, F. Perreault, S. Garcia-Segura, Sci. Total Environ. 737 (2020) 140044.
[45] M. Zu, X. Zhou, S. Zhang, S. Qian, D.-S. Li, X. Liu, S. Zhang, J. Mater. Sci. Technol. 78 (2021) 202–222.
[46] H. Wang, L. Hu, W. Han, J. Alloy. Compd. 854 (2021).